A New Madrid Seismic Zone Fault System Model from Relative Event Locations and Application of Optimal Anisotropic Dynamic Clustering

Yixin Zhang[1], Oluwaseun Fadugba[1], Christine Powell[1], Stephen Horton[1], and Charles A. Langston[1]

[1]Center for Earthquake Research and Information, The University of Memphis, Memphis, TN

Corresponding author: Yixin Zhang (yzhang22@memphis.edu)

Key Points:

- New Madrid seismic zone hypocenters for the years 2000-2019 are relocated and have a median location error of 65m.
- Planes are fit to the relocated hypocenters producing a detailed three-dimensional model of fault structure.
- The Reelfoot fault is segmented along its length.

Abstract

A new model of fault structure in the active New Madrid Seismic Zone (NMSZ) is presented based on relocated hypocenters and application of a statistical clustering method to determine fault planes. Over 200 earthquakes are recorded in the NMSZ every year, but the three-dimensional (3-D) fault structure is difficult to determine because the zone is covered by thick, Mississippi Embayment sediment. The distribution of earthquakes in the NMSZ indicates four major arms of seismicity, suggesting the presence of a northeast-southwest trending strike-slip fault system with a major northwest trending, contractional stepover fault. The most seismogenic faults are the strike-slip Axial fault and the Reelfoot thrust fault. Developing an accurate, 3-D fault model is important for dynamic modeling of the fault system and better specification of the seismic hazard. We relocated 4131 hypocenters for earthquakes occurring between 2000 and 2019 using the HypoDD double difference relocation technique. HypoDD is appropriate for the NMSZ because the earthquakes are tightly clustered, and the network stations are dense. The Optimal Anisotropic Dynamic Clustering technique is used to develop the fault structure for the NMSZ using the relocated hypocenters. The Reelfoot fault is continuous along strike from the northern end to the Ridgely fault, located south of the intersection with the Axial fault. The strike-slip arms are well resolved and correspond to near vertical planes. Three planes are resolved in the southern part of the Axial fault and are associated with the Osceola intrusive complex.

Plain Language Summary

A new fault model is determined for the active New Madrid seismic zone using earthquakes that occurred from 2000 to 2019. The seismic zone is located in the central United States and poses a hazard to critical infrastructure and numerous population centers. The major faults are the

Reelfoot thrust fault and the strike-slip Axial fault. The first step in constructing the improved fault model involved relocation of the earthquakes to decrease location error. The second step involved fitting planes to the relocated earthquakes under the assumption that the earthquakes cluster along fault segments. The resulting model provides a three-dimensional representation of the fault structure. A major fault disrupts the southern portion of the Reelfoot fault, making it discontinuous. The northern part of the Axial fault is very well defined. Earthquakes are more scattered along the southern part of the Axial fault, but three fault planes are resolved that are located along the side of a major intrusion. The fault model can be used in studies involving possible rupture length and magnitude of large earthquakes.

1 Introduction

The intraplate New Madrid Seismic Zone (NMSZ) is located in the northern Mississippi Embayment (ME) (Figure 1). Over 200 NMSZ earthquakes are recorded every year but the zone is most noted for three large earthquakes (M>7) that occurred in 1811-1812 (Johnston, 1996; Hough et al., 2000). Present seismicity is not a prolonged aftershock sequence from the 1811-1812 events (Page and Hough, 2014) and is being driven by ongoing strain accumulation. Determining the reason for the buildup of strain is hampered by very low strain rates on the order of 10^{-9} yr^{-1} indicated by global positioning studies (GPS) (Calais and Stein, 2009; Frankel et al. 2012, Boyd et al. 2015). The 1811-1812 sequence was not unique; paleoseismic evidence suggests that large NMSZ earthquakes occur roughly every 500 years (Tuttle et al., 2002; 2019). A few models for strain accrual, particularly those involving relaxation of a weak lower crust or upper mantle (Kenner and Segall, 2000; Zhan et al, 2016) and dislocation creep on the lower portion of the major thrust fault (Frankel et al., 2012) reproduce the GPS observations with a

high degree of fidelity. Geological observations suggest that slip rates on NMSZ faults have increased in the Holocene, reaching 4.4-6.2 mm/yr (Mueller et al., 1999; Van Arsdale, 2000).

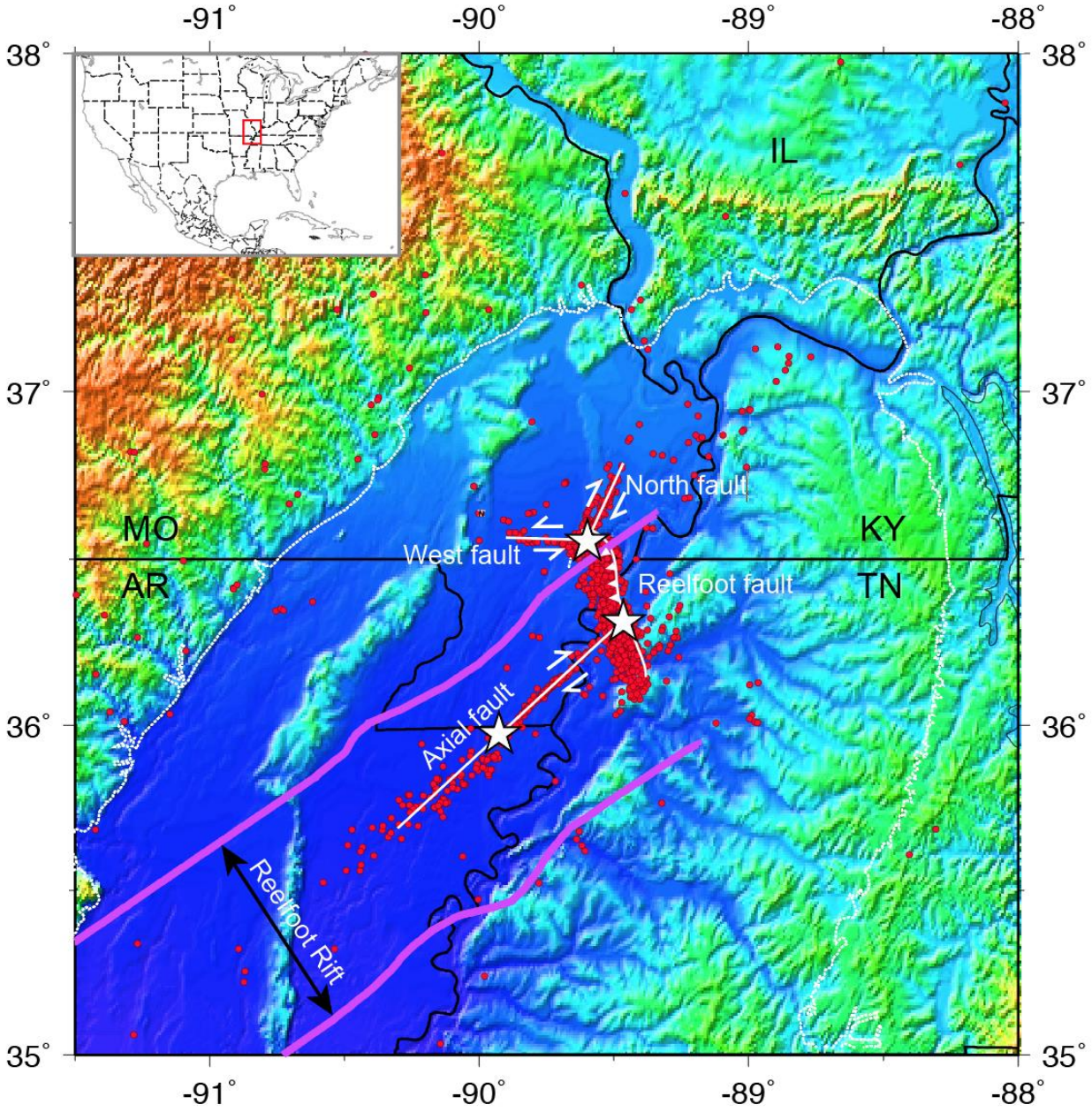

Figure 1. Seismicity (red circles) in the NMSZ and nearby areas compiled by the Center for Earthquake Research and Information catalogs from April 1974 to December 2012. Three white stars are paleo-earthquakes with a magnitude over M 7.0 (Johnston and Schweig, 1996; Hough et

al., 2003). Magenta lines indicate the boundary of the Reelfoot Rift. White dashed line is the boundary of the Mississippi Embayment. The inset map shows the location of the present study area (red box). Basic NMSZ fault geometry and offsets are indicated by white lines. MO: Missouri; IL: Illinois; KY: Kentucky; TN: Tennessee; AR: Arkansas. (modified from Dunn et al., 2013).

Four major fault arms in the NMSZ are illuminated by the distribution of seismicity (Figure 1): a vertical left-lateral strike-slip fault (West fault, WF) with a strike of about 270° to 280°, a vertical right-lateral strike-slip fault (North fault, NF) with a strike of about 25° to 30°, a vertical right-lateral strike-slip fault (Axial fault, AF) with a strike of about 40° to 50° and an approximately northwest-southeast trending thrust fault (Reelfoot fault, RF). The RF is divided into northern and southern parts near the intersection with the AF (Figure 1). The northern segment is interpreted as a compressive stepover between the right lateral AF and NF strike slip faults (e.g., Pratt, 2012). The presence of the southern segment of the RF is difficult to define in terms of a simple structural model and this segment is cut by at least one northeast trending fault (Csontos and Van Arsdale, 2008).

Accurate fault models are needed to properly assess the hazard that the NMSZ poses to the central United States. The most detailed three-dimensional (3-D) fault model was developed by Mueller and Pujol (2001) based on the distribution of about 550 relocated NMSZ hypocenters. This study centered on the RF and divided the fault into northern, central, and southern segments. Structural contours of the thrust surface were determined by dividing the fault into strips oriented perpendicular to the local fault strike, projecting the earthquakes in each strip to the center line and fitting the fault surface by hand. The resulting model captured the

change in strike along the RF from about N28°W in the south, to NS in the center, to N10° to 20°W in the north. The dip on the southern portion of the fault is steeper than on the northern portion.

In this study, we will determine a more complete fault model for the NMSZ that includes the strike-slip arms of seismicity as well as the RF. HypoDD (Waldhauser and Ellsworth, 2000) will be used to relocate NMSZ earthquakes recorded between 2000 and 2019. Optimal Anisotropic Dynamic Clustering (OADC) will be used to generate three-dimensional (3-D) fault structure, under the assumption that hypocenters cluster along fault surfaces. Ouillon et al. (2008) applied OADC to the 1992 Landers California earthquake aftershock sequence and arrived at a successful match between modeled fault structure and known faults based on geological mapping (Ouillon et al., 2008). The technique was used by Hardebeck (2013) to investigate the geometry of the Shoreline fault near San Luis Obispo, California and most recently by Fadugba (2021) to delineate fault structure in the Charlevoix seismic zone. The large number of earthquakes and the high station density make the NMSZ an excellent candidate for OADC analysis. We will use OADC to cluster the relocated hypocenters and create a reasonable fault model for the NMSZ that specifies fault locations, dimensions, and strike and dip angles.

1.1 Tectonic History

During the supercontinent Rodinia fragmentation in the early Paleozoic, several grabens, including the Reelfoot Rift, were generated in Precambrian basement rock, inboard of the rifted margin (Thomas, 1991; Thomas, 2006). The extension thinned and weakened the ME lithosphere possibly leading to mafic intrusions in the lower crust. The rift was compressed during the late Paleozoic Ouachita orogeny. Uplifts, including the Pascola arch roughly coincident with the RF,

occurred and some intrusions may have been emplaced along the rift axis and margins. The thinned lithosphere below the rift allowed upwelling of high-temperature fluid during passage of the Bermuda hotspot in the Cretaceous (Cox and Van Arsdale, 1997; 2002). Intrusions along the axis and margins of the rift were also emplaced during this time and passage of the hotspot may have resulted in formation of the ME (Cox and VanArsdale, 1997; 2002). Thick, unconsolidated Upper Cretaceous and younger sediments cover the ME (Cox and Van Arsdale, 2002; Hildenbrand and Hendricks, 1995) and make it difficult to determine the faulting kinematics. The only surface expression of faulting in the NMSZ is the Reelfoot scarp, a 32 km long uplift that is associated with the RF thrust. The scarp has up to 9m of structural relief due to monoclinal flexure (Mueller et al., 1999). Widespread sandblows attest to the occurrence of strong, repeating earthquakes in the zone (e.g., Tuttle et al., 2002; 2019). Uplift rates may have increased in the Holocene in the NMSZ and along the eastern rift margin based on seismic reflection interpretations (Van Arsdale, 2000; Hao et al., 2013).

2 Data

Broadband data were obtained from the Center for Earthquake Research and Information (CERI) earthquake catalog. We used earthquakes recorded from Jan 1st, 2000 to Dec 31st, 2019 within an area from $35.5°N$ to $36.9°N$ and from $90.6°W$ to $89.2°W$ (Figure 2). This dataset includes 4568 earthquakes recorded by 314 stations.

Waveform cross-correlated data were generated using a program developed by Horton et al. (2005). We eliminated any CC event that was paired with less than eight events and the threshold for the cross-correlation coefficient was set to 0.7. This resulted in a cross-correlation catalog containing 4486 earthquakes.

3 Methods

3.1 Double-Difference (DD) Relocation

The velocity structure associated with the NMSZ is complex and the double difference inversion method of Waldhauser and Ellsworth (2000) will minimize the effects of unmodeled velocity heterogeneity when determining earthquake relocations. HypoDD takes advantage of dense earthquake and station distributions which makes the NMSZ an excellent candidate for the method.

We used the HypoDD program to determine the relative relocations. Each input event was linked with at least 8 neighbor events within a 10 km radius. The double-difference travel time residuals were calculated for each pair of events and minimized in the inversion process using either the conjugate gradient method (LSQR, Paige, 1982) or singular value decomposition (SVD). For both inversion approaches, HypoDD minimizes the residuals between the observed arrival time differences from paired stations and the calculated differences by updating the hypocenters and reweighting the data iteratively, until the residual becomes lower than the noise level or until the number of iterations reaches a preset limit (Waldhauser and Ellsworth, 2000).

3.1.1 LSQR inversion

LSQR is efficient when dealing with a large number of sparsely located events; it can be used to analyze a large hypocentral system by solving the damped least-square problem. HypoDD uses damping to regularize the solution. A condition number (CND), representing the

160 stability of the system, is returned as well as a root-mean-squared residual (RMS) time for the
161 solution in milliseconds. The damping factor should be in the range 1 to 100 and reasonable
162 CND values should lie between 40 and 80.

163 To improve the LSQR results, we partitioned the NMSZ events into 8 clusters according
164 to their probable kinematic structure (Figure 2). Clusters 1, 2 and 6 represent the three strike-slip
165 faults, the WF, NF and the AF. Events in cluster 7 are more scattered than those in cluster 6 and
166 they are therefore placed into a separate cluster. Clusters 3, 4 and 5 together cover the main RF.
167 We separated the RF into 3 clusters because prior research indicates that the three segments have
168 different strike and dip angles (Mueller and Pujol, 2001; Parrish and Van Arsdale, 2004; Csontos
169 and Van Arsdale, 2008; Pratt, 2012; Greenwood et al., 2016; Delano et al., 2018). Cluster 8
170 contains events at the intersection of clusters 1, 2 and 3, that cannot be placed into any of the
171 other clusters.

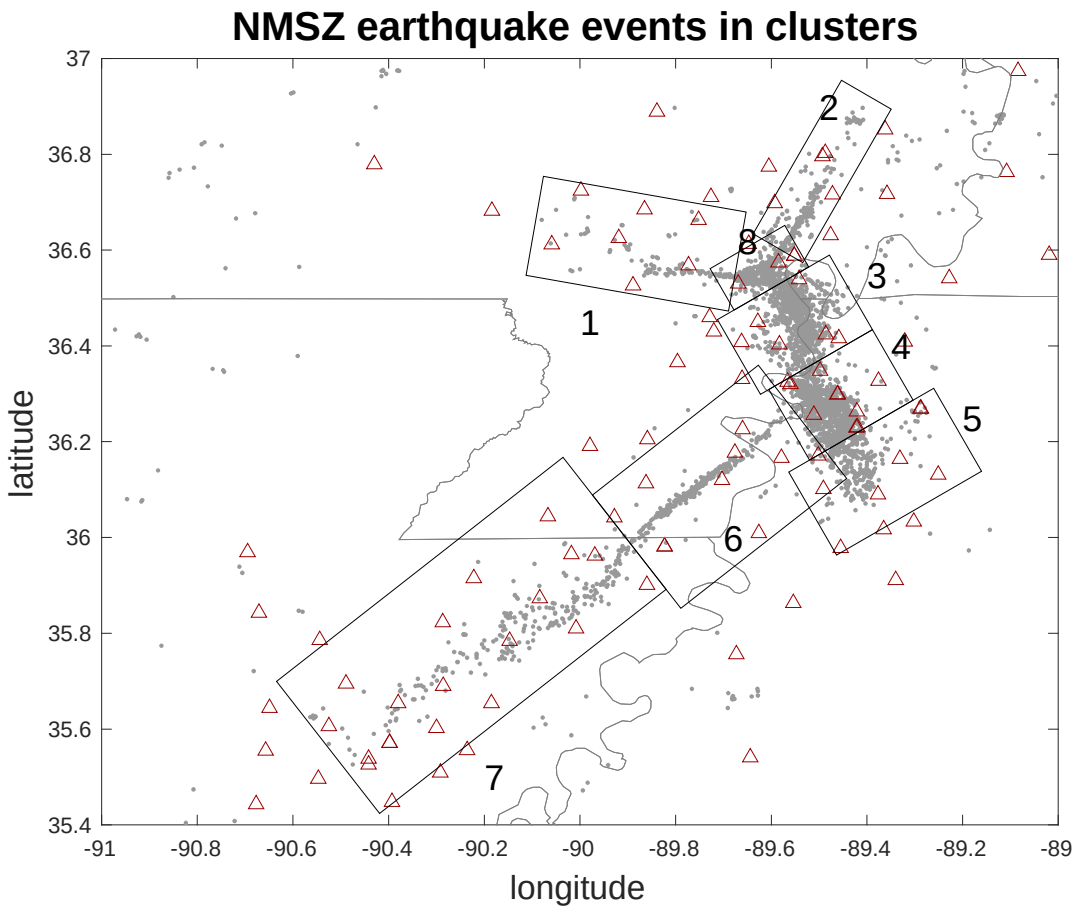

Figure 2. Partitioning used for the HypoDD relocation analysis. Grey dots are the NMSZ earthquakes. Red triangles are NM seismic stations. State boundaries are indicated. Black boxes separate earthquakes into 8 clusters based on fault type and prior studies indicating segmentation along the RF.

The HypoDD program can use any combination of original phase-picked earthquake catalog times and waveform cross-correlated differential times (Waldhauser and Ellsworth 2000). Users can set different weights for each dataset in any iteration. Original phase-picked catalog data (catalog data; CT) are more numerous than the waveform cross-correlated catalog

data (cross-correlation data; CC), while the CC data are more accurate. To test the stability and quality of the NMSZ data, we ran HypoDD with LSQR using the CT data only and then using CC data only. For both datasets, we ran the inversion for the 8 separate clusters shown in Figure 2 and then combined the results. This produced 4422 event relocations with a median RMS residual of 60 milliseconds for the CT data and 2647 event relocations with a median RMS residual of 38 milliseconds for the CC data (see Supporting Information Figures S1 and S2).

Based on both the CT and CC data results using HypoDD with LSQR, we tested several sets of data weights and determined the appropriate weights as indicated in Supplementary Table S1. For the first 2 iterations, we weighted CT data higher to include more event information. For the following iterations, we increased the weights for the more accurate CC data. S waves are generally less accurate than P waves, thus we lowered the weights of the S waves for both data types (CT and CC). After applying the weights in Table S1 and adjusting damping parameters for the 8 clusters, a set of CND numbers and RMS residual times for both types of data were generated and listed in Supplementary Table S2. With one small exception for cluster 3, the CND numbers are within the reasonable range (40 to 80). The damping values used for clusters 3, 4 and 8 are high, which may indicate low stability for these clusters. Supporting Information Figure S3 indicates that relocation using both types of data (CT and CC) results in a much smaller RMS residual than using CT data alone.

3.1.2 SVD inversion

The SVD method is applied to the combined CT and CC data. The SVD method can only process a small number of events (we used 50 in our study) but gives more accurate solutions (smaller residuals) than LSQR along with relocation errors. The SVD approach is more efficient when examining small hypocenter datasets. To use SVD, we first roughly partitioned events by their locations into *a* by *a* (*a*=0.2 rad degree) sized blocks. To make sure each block has less than 50 events, we continuously partitioned blocks which have more than 50 events into 4 equally sized blocks. The smallest blocks have a size of *a*/64 by *a*/64. Then, HypoDD was run using SVD for each block to obtain event relocations and the associated errors in meters. The process of event partitioning can cut off events from their linked neighbor events and prohibit them from pairing with other events in adjacent blocks. To compensate for the loss, we shifted the starting point of the partitions to the northeast at lengths of $\frac{\sqrt{2}}{2}a$, $\frac{\sqrt{2}}{4}a$, $\frac{\sqrt{2}}{8}a$, $\frac{\sqrt{2}}{16}a$, $\frac{\sqrt{2}}{32}a$, $\frac{\sqrt{2}}{64}a$, $\frac{\sqrt{2}}{128}a$ and ran the inversion 7 more times, so that most of the blocks are overlapped by different blocks at least once. In the end, we used the location with the smallest error for each event. A comparison between the LSQR and SVD results is presented in the Supplemental Material. The SVD results are used for the OADC analysis.

3.2 Optimal Anisotropic Dynamic Clustering

OADC (Ouillon et al., 2008) is a planar fault recognition technique to determine 3-D fault structure from the spatial distribution of hypocenters in a region with elevated seismicity. It is a generalization of the dynamic clustering method (or *k*-means clustering method (Likas et al., 2003)) which partitions *n* observations into *k* clusters using the variance of the observations about their center of mass (barycenter) as a global minimization criterion. Specifically, the *k*-

means method involves first setting *k* initial centroid points randomly and then calculating the distances between each observation and each initial point. The *n* observations are then clustered into *k* groups where, in each group, the observations share the same nearest centroid. A new set of centroid points are appointed by using the calculated mean point of each cluster. The clustering will run iteratively until a configuration is reached that produces the smallest variance (Likas et al., 2003).

Ouillon et al. (2008) develop a minimization criterion that takes into account the whole covariance tensor of each cluster, leading to the concept of 3-D dynamic clustering. The fault planes for each cluster are determined using principal component analysis of the covariance tensor to develop optimal fault geometries. Following the *k*-means approach, the hypocenters are partitioned into different clusters based on their proximity to an initial, random fault(s). Eigenvalue-eigenvector analysis of the covariance matrix of each cluster is used to determine the dimensions and orientation of the optimal fault plane. The whole covariance matrix of a cluster is

$$C = \begin{pmatrix} \sigma_x^2 & cov(x,y) & cov(x,z) \\ cov(x,y) & \sigma_y^2 & cov(y,z) \\ cov(x,z) & cov(y,z) & \sigma_z^2 \end{pmatrix}.$$

Assume λ_1, λ_2, λ_3, $\boldsymbol{u}_1$, $\boldsymbol{u}_2$, $\boldsymbol{u}_3$ are eigenvalues and eigenvectors, respectively, obtained by diagonalizing the covariance matrix C. The largest eigenvalue λ_1, refers to the length of the 3-D cluster (i.e., fault plane length), λ_2, refers to the width of the fault plane and λ_3, refers to the thickness.

If earthquakes are uniformly distributed over a fault of length L and width W then $L=\lambda_1\sqrt{12}$ and $W=\lambda_2\sqrt{12}$ (Ouillon et al., 2008). The square root of λ_3 is the standard deviation of

245 the location of the earthquakes perpendicular to the fault plane and should be on the order of the
246 location uncertainty. In addition, $\boldsymbol{u}_3$ is the pole to the plane and specifies the strike and dip of the
247 fault. Following the *k*-means method, the hypocenters are partitioned again after the first
248 iteration into different clusters using the updated fault geometries. The algorithm is repeated for
249 the initial number of faults until the faults converge to a fixed geometry (i.e., the maximum value
250 of λ_3 is smaller than an allowable thickness). The objective is to partition the hypocenters by
251 minimizing the sum of all λ_3 values obtained for each clustering so that the partition will
252 converge to a set of clusters that tends to be as thin as possible in one direction while being
253 arbitrary in the other directions. A maximum number of clusters is set to account for the
254 possibility that the program will fail to converge. The OADC method tends to find a near
255 horizontal plane for a cluster that consists of hypocenters in a small depth range relative to the
256 horizontal area (Ouillon et al., 2008; Ouillon and Sournette, 2011; Hardebeck, 2013). Thus, a
257 constraint is placed on the dip angle to avoid modeling subhorizontal planes.

258 The OADC program we used was developed by Fadugba et al. (2019). Hypocenter errors
259 from the original catalog were used to set the maximum thickness of the fault planes, λ_3, to 1.2
260 km. Using smaller errors determined by the HypoDD analysis prevented the program from
261 converging. A similar problem was encountered by Ouillon et al. (2008) in the analysis of the
262 Landers, California earthquake aftershocks and the original catalog error was used in that study.
263 The program output includes the spatial dimensions, orientation and location for each fault plane.
264 We set the maximum number of possible planes to 100 and we set a minimum dip angle of 10°
265 to avoid generating subhorizontal planes. The simulation ran 5 times for each increment in the
266 number of fault planes to improve the convergence success rate and we chose the result that has
267 the minimum λ_3.

3.3 Declustering Analysis

We removed outlying hypocenters from clustered hypocenters prior to the OADC analysis to facilitate identifying accurate fault planes. We used a declustering program developed by Fadugba (2021) that is based on the cumulative tetrahedra volume method of Ouillon and Sornette (2011). A detailed description is presented in Fadugba (2021). Briefly, a randomized catalog of events for a particular portion of the NMSZ was generated. We determined the volume of tetrahedra formed with quadruplets of nearest neighbor events for each hypocenter for both the observed and randomized catalogs. After determining the cumulative distributions of the volumes of the observed and randomized catalogs, we separated the diffuse earthquakes from the observed earthquakes by removing all hypocenters in the observed catalog with volumes above a certain volume threshold. Following Fadugba (2021), we use the 5% quantile as the maximum threshold of the tetrahedra volume distribution to model the diffuse earthquakes

4 Results

4.1 Relocation

Relocations determined using HypoDD with SVD are shown in Figure 3. As is indicated in the histogram (Figure 3b), the mode of the residual time is located in the 10 to 15 ms range. About 1800 events have an RMS residual below 15 ms. A comparison between original catalog hypocenters and relocated hypocenters for each group in Figure 3 is presented in Supporting Information Figure S4. The SVD solution also returns the error in meters for event relocations. The accuracy of earthquake locations in the NMSZ is significantly improved using HypoDD as can be seen in Supporting Information Figure S5, showing the original event errors and the

relocated event errors. Relocated events in the NMSZ have a minimum error of 11m, a median error of 65m, and a mean error of 110m. This is a significant reduction of hypocenter uncertainties from the original uncertainties averaging about 1 km. The RMS residuals for the HypoDD solution for each cluster shown in Figure 2 are plotted in Figure 4. Clusters 4, 5 and 6 contain the smallest RMS residuals, indicating more stable hypocentral relocations than in the other clusters.

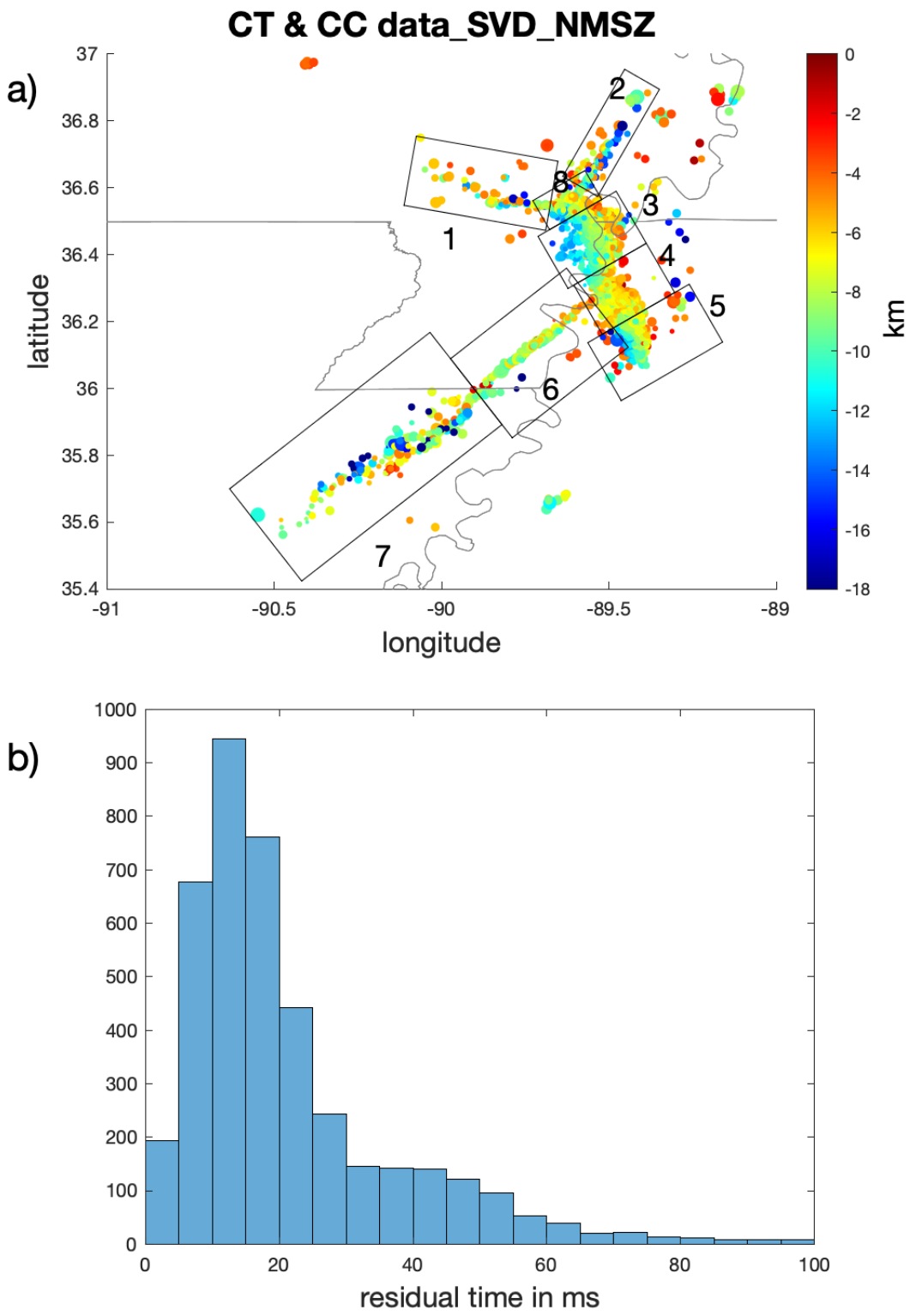
CT & CC data_SVD_NMSZ
a)
latitude
longitude
km
1
2
3
4
5
6
7
8
b)
residual time in ms

296

297 **Figure 3.** (a) NMSZ event locations determined using HypoDD using both catalog data and
298 cross-correlated data. Circles represent earthquakes; the size of circles is proportional to the
299 earthquake magnitude, ranging from 0.1 to 3.9. The color scale shows the hypocenter depth. (b)
300 Histogram of the residual times for the 4131 events.

301

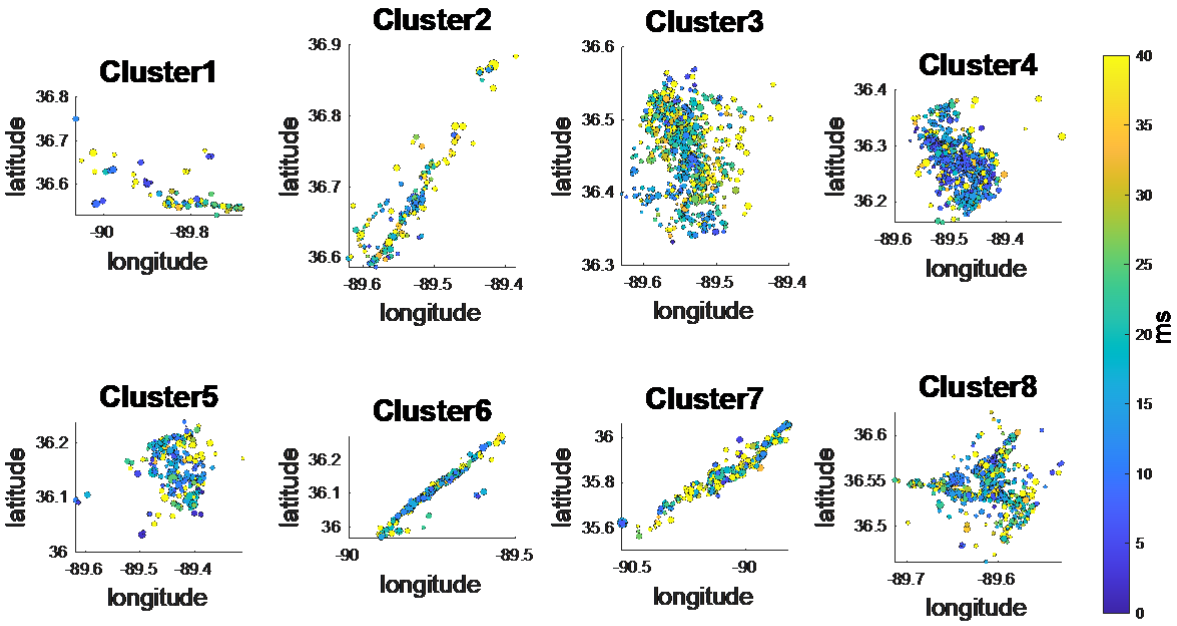

302

303 **Figure 4.** NMSZ event relocations determined using HypoDD using both catalog data and cross-
304 correlated data in each cluster. The color scale is the RMS time residual.

305

306 The relocated hypocenters in Figure 3 provide a detailed view of structure on the RF.
307 The northern and southern parts of the fault (clusters 3 and 5) have the least complicated
308 structure and are clearly dipping to the southwest. The dip on the southern part is steeper than the
309 dip on the northern part, in agreement with the assessment by Mueller and Pujol (2001).

Structure in the middle part of the RF (cluster 4) is more complex and the fault is not as deep as the northern and southern parts. A shallow, crosscutting, northeast-trending fault is present in this cluster as indicated by the orange band of seismicity. The northern part of the AF (cluster 6) is very well defined and does not extend deeper than about 10 km. The fault is shallower near the intersection with the RF, possibly indicating more structural complexity.

4.2 OADC fault models

The spatial dimensions of the NMSZ fault system make it difficult to use OADC modeling for the whole NMSZ; the horizontal extent of the seismic zone is much larger than the vertical extent, giving it a flat shape and OADC will tend to model this as a flat fault. To avoid this problem, we separated the NMSZ into 3 areas, the northern part (NP) containing the WF and NF and the intersection of WF and NF and RF, the remaining RF part (RFP), and the AF part (AFP). The separate parts are shown in Figure 5 along with the results of the declustering analysis.

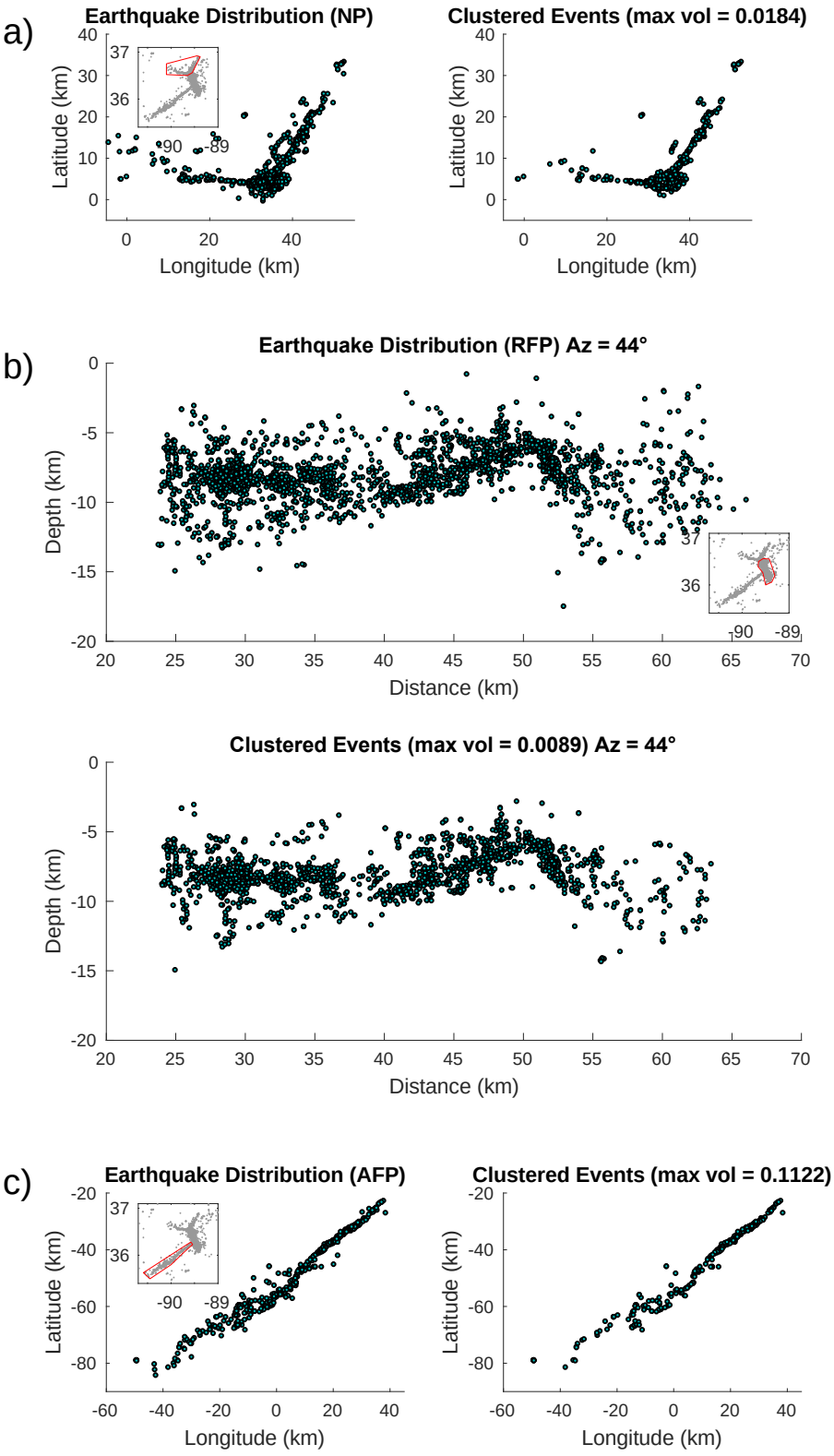
a)
Earthquake Distribution (NP)
Clustered Events (max vol = 0.0184)
Latitude (km)
Longitude (km)
b)
Earthquake Distribution (RFP) Az = 44°
Clustered Events (max vol = 0.0089) Az = 44°
Depth (km)
Distance (km)
c)
Earthquake Distribution (AFP)
Clustered Events (max vol = 0.1122)

Figure 5. Relocated and declustered NMSZ seismicity. Northern Part (NP), Reelfoot Part (RFP), and the Axial Fault Part (AFP) . The left are relocated earthquakes before declustering and the right are the associated remaining hypocenters after declustering. RFP is shown as viewed from an azimuth of 44°. For each area, we use the 5% quantile as the maximum threshold of the tetrahedra volume distribution to model the diffuse earthquakes (see Fadguba 2021). The maximum tetrahedra volume in km^3 for each area is labeled in the bottom figures (Ouillon and Sornette, 2011).

Since the starting plane and added planes in each increment of the OADC modeling are random, the resulting fault models will be different for each run. Two runs for the RFP are shown in Figure 6 as an example. Both models have the main fault plane indicating a northwest trending, southwest dipping thrust fault. However, the sizes of the thrust fault planes in the two models are different, as well as their locations and their strike and dip angles. Some minor faults that pass through the main faults are present in both models, and some are quite different from each other. Due to the complexity of the NMSZ, we ran 500 models for each of the three parts shown in Figure 5. There were 208, 383, and 218 models that converged within the threshold thickness λ_3 = 1.2 km for the NP, RFP, and AFP, respectively. For faults that appear in several successful model results, we calculate their average plane strike and dip angles (all strike and dip angles follow the right-hand rule), location, width, length and thickness. We remove randomly distributed faults that just occur in a few models. We also plot the centers of the acceptable fault planes to examine the tendency of the hypocenters to cluster into faults (Figure 7).

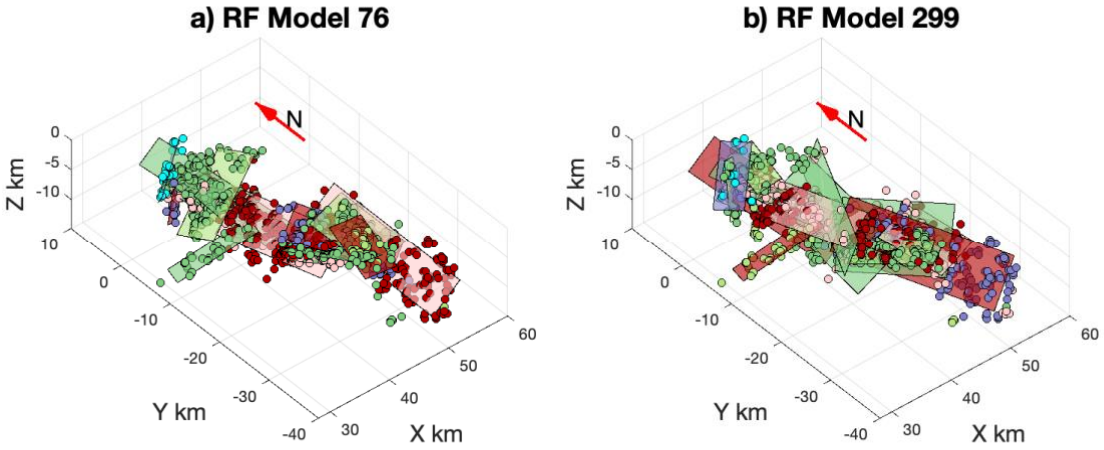

345

346 **Figure 6.** Two fault models for the RF area. The main RF thrust fault shows up striking to
347 northwest and dipping to the southwest in both models, as well as some minor faults, such as the
348 long-narrow fault intersecting the north RF area.

349

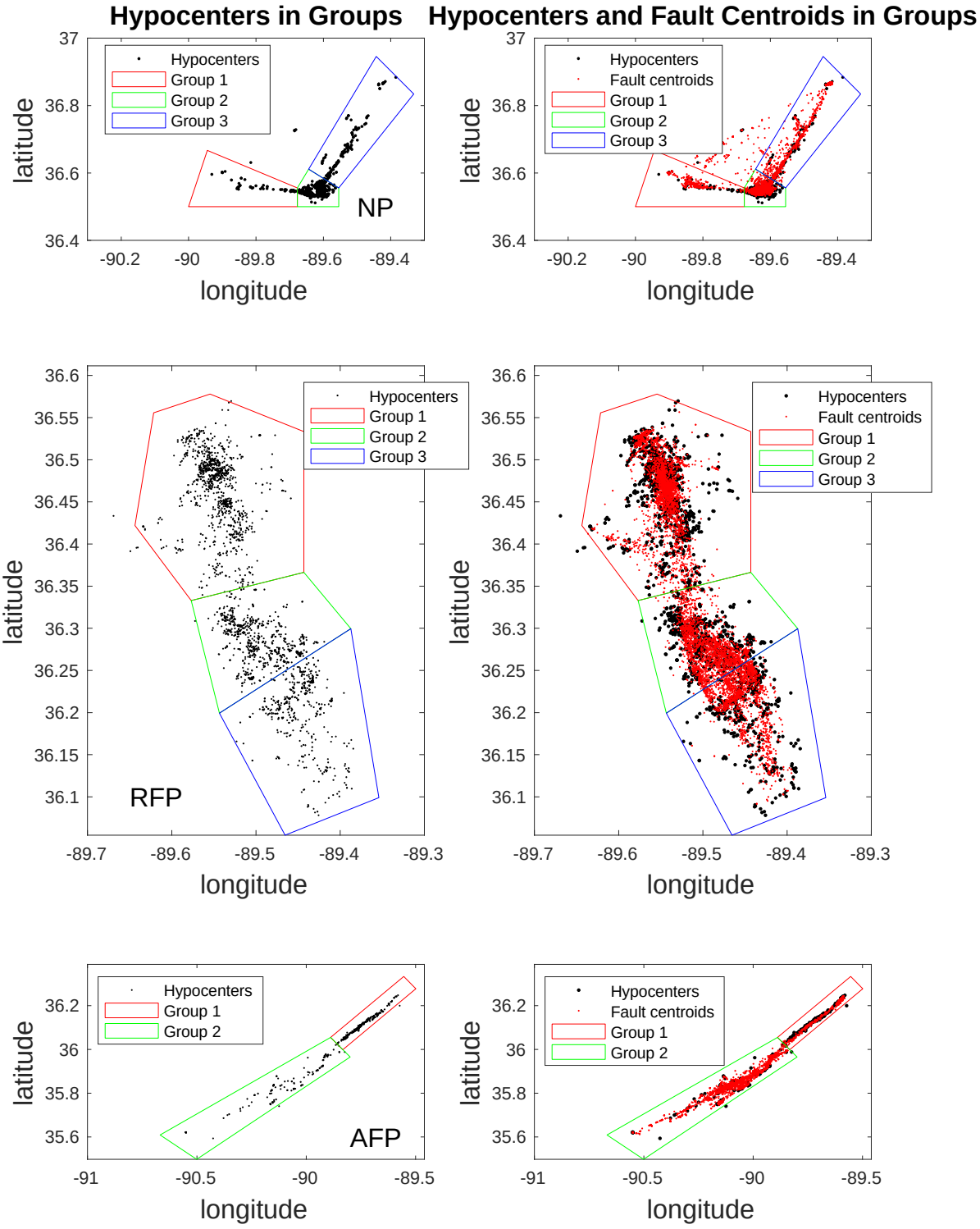
Hypocenters in Groups
Hypocenters and Fault Centroids in Groups
Hypocenters
Fault centroids
Group 1
Group 2
Group 3
NP
RFP
AFP
latitude
longitude

Figure 7. Left) The three areas for OADC analysis and how they are subdivided into groups. Right) black dots are earthquakes; red dots are the centroids of all resolved fault planes from every model that converged.

We subdivide each area in Figure 5 into groups based on the distribution of seismicity (Figure 7). The analysis of the RFP, the most seismogenic part of the NMSZ is presented in Figures 8-10 and is discussed in detail below. OADC analysis for the NP and AFP areas are in the Supporting Information (Figures S6 – S10). As indicated in Figures 8–10, we plot the results from all of the successful models and show a histogram of fault strikes and a rose diagram of dip angles for each group. We determine the mean strike for any peak in the histogram with more than 40 values within a range of clustered strikes and the mean dip angle. This analysis produced 31 fault planes total for the three areas (RFP, NP and AF). Fault parameters for the 31 planes are given in Supplementary Table S3. A final fault model is determined by using only those faults with 200 or greater modeled planes, as indicated in Table 1. We determined each final fault center by using the mean center of their related modeled planes. Then, by using the mean width as the width of the final average fault and the mean length as the length of the final fault, the size of one final average fault is determined. Applying those final planes along with their mean strike values and mean dip angles, we established our final fault system for NMSZ (Figure 11).

Table 1. PARAMETERS OF MODELED FAULT PLANES

Part name	Group #	Fault ID	Strike range	Dip range	X mean value	Y mean value	Z mean value	Strike mean value	Dip mean value	Length mean value	Width mean value	Lambda 3 mean value	# of modeled planes
Northern	2	8	80~125	75~90	32.2	3.7	-8.1	96	86	11.4	4.0	0.9	242

	3	10	30~50	75~90	41.8	15.8	-9.3	34	83	18.0	5.1	0.9	288
RF	1	18 (North RF)	140~230	15~45	41.0	-4.4	-8.4	172	31	15.8	5.8	0.9	1513
	2	19	100~135	0~30	47.2	-20.8	-6.3	119	18	12.2	6.1	1.0	215
		20	135~165	30~60	46.2	-20.3	-7.5	150	44	14.7	6.0	0.9	312
		21	165~205	15~45	43.9	-18.1	-7.9	185	30	13.5	5.5	0.9	464
	3	23 (Ridgely fault)	20~65	30~75	48.9	-24.6	-6.9	44	52	8.2	4.2	0.8	207
		24 (South RF)	100~170	30~60	49.9	-26.8	-8.3	148	45	15.8	6.2	1.0	682
AF	1	26	40~70	75~90	22.1	-35.4	-8.1	52	84	21.2	3.9	0.9	296
	2	28	10~90	50~65	-5.5	-57.8	-7.7	50	57	10.8	2.7	0.5	218
		29		70~90	-8.4	-59.6	-8.6	49	82	13.8	4.0	0.7	547
		30	210~270	75~90	-12.0	-61.3	-12.1	239	85	16.7	4.4	0.6	681

371

372

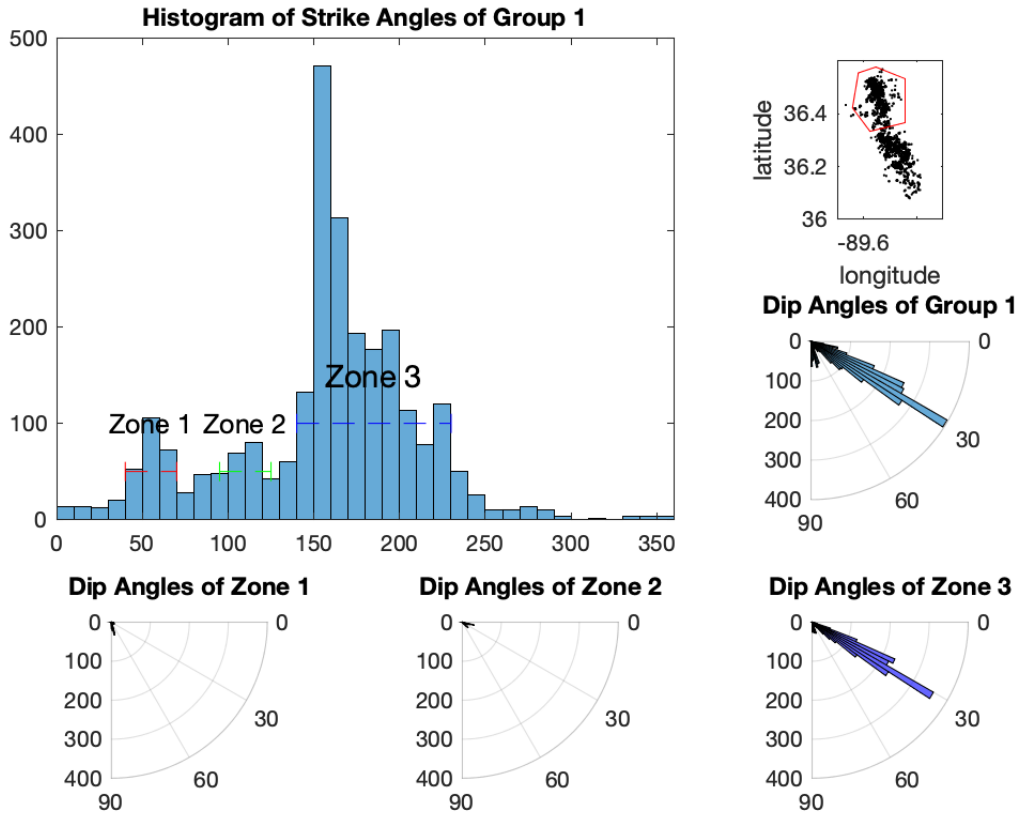

373

374 **Figure 8.** OADC analysis for RFP group 1 (upper right). Three zones are labeled with bin values
375 over 40. The dashed lines indicate the strike range for each zone. Rose diagrams are determined
376 for each zone. Fault parameters for these zones are given in Table S3. Only zone 3 is used in the
377 final fault model.

378

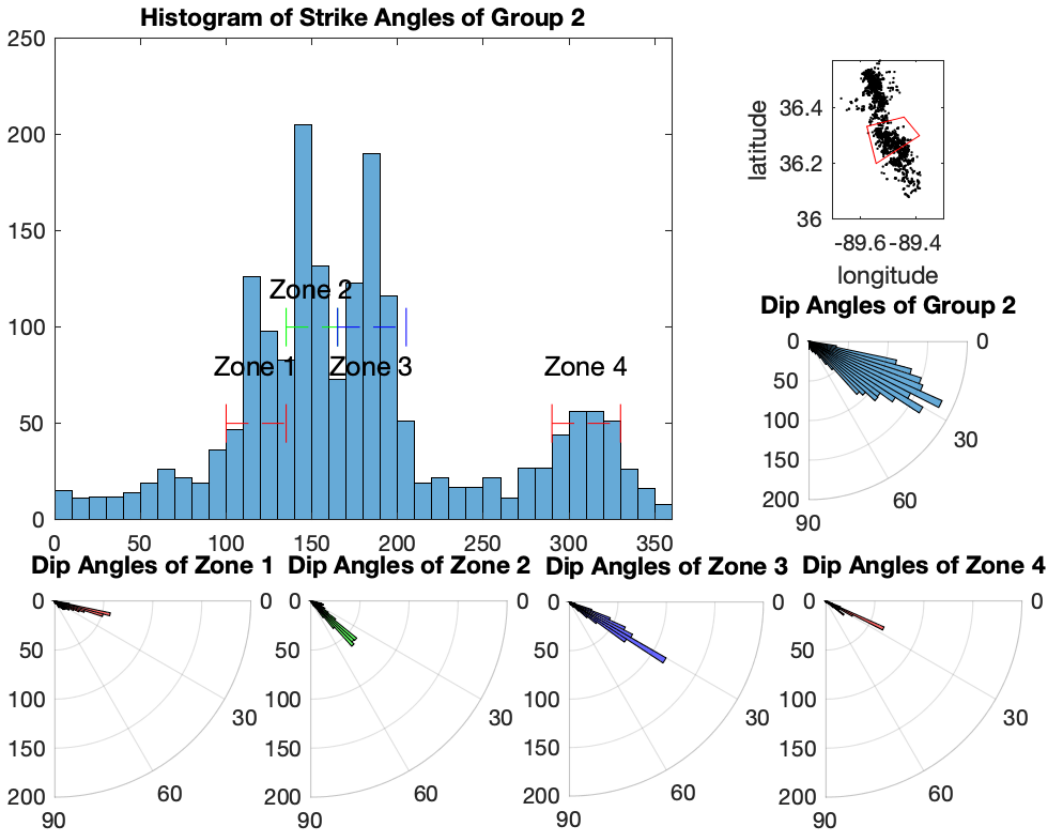

379

380 **Figure 9.** OADC analysis for RFP group 2 (upper right). Four zones are labeled with bin values
381 over 40. The dashed lines indicate the strike range for each zone. Rose diagrams are determined
382 for each zone. Fault parameters for these zones are given in Table S3. Zones 1-3 are used in the
383 final model.

384

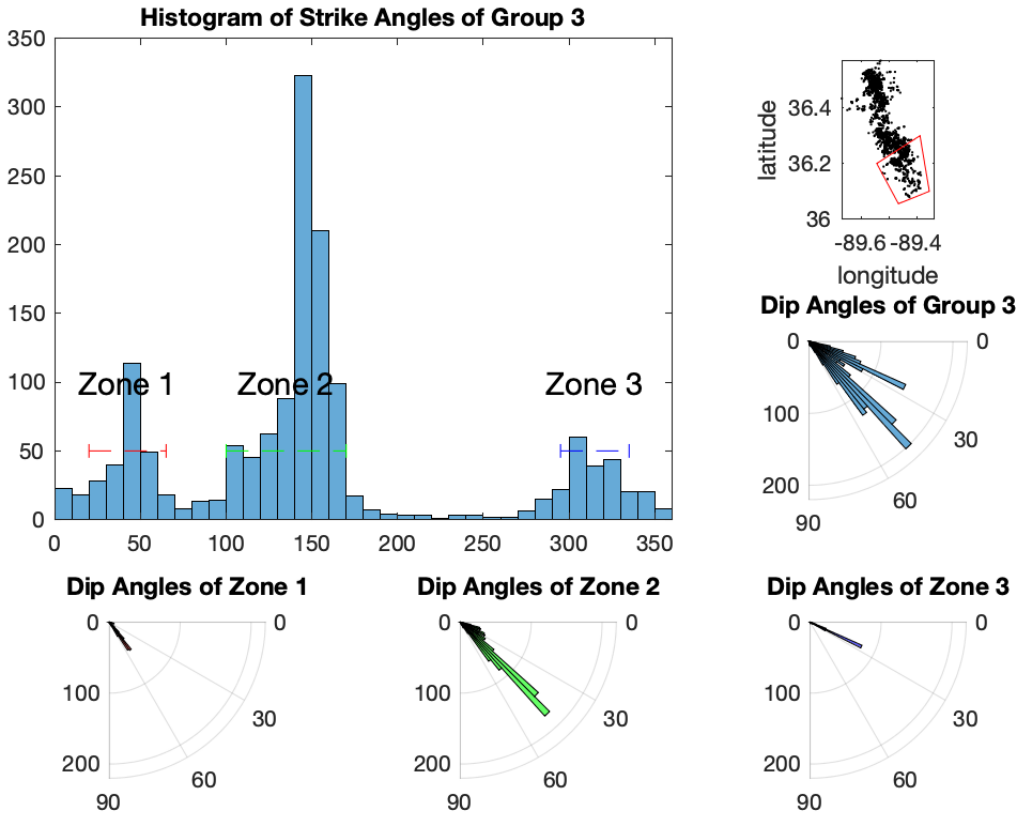

385

386 **Figure 10.** OADC analysis for RFP group 3 (upper right). Three zones are labeled with bin
387 values over 40. The dashed lines indicate the strike range for each zone. Rose diagrams are
388 determined for each zone. Fault parameters for these zones are given in Table S3. Zones 1 and 2
389 are used in the final model.

390

391 RFP Group 1 (Figure 8) contains the northern part of the RF. The modeled average fault
392 for zone 3 has a strike of N172° and a dip angle of 31°, in agreement with a strike of N160° to
393 170° determined in previous studies (Parrish and Van Arsdale, 2004; Csontos and Van Arsdale,
394 2008; Greenwood et al., 2016). Strikes and dips of the planes in zone 1 suggest the presence of

steeply dipping faults that crosscut the trend of the northern RF. However, only the average fault plane from zone 3 in group 1 is used in the final fault model (fault 18 in Table 1).

Group 2 (Figure 9) has the most complex fault structure in the NMSZ. The strike distribution is broader than the distribution found for group1, but the pattern is similar. The major exception is the presence of zone 4 in group 2. The strike directions for most planes in zone 4 are the same as those for zone 2 but the dip directions are different. This suggests the presence of backlimb or kink bend faults as suggested in previous studies (e.g., Mueller et al., 1999). Fault planes representing zones 1 – 3 (faults 19, 20, and 21 in Table 1) are used in the final model.

The main fault in group 3 (Figure 10) has a mean strike of N148° and a mean dip of about 45°. This corresponds to strikes of N150°~160°determined for the southern RF in previous studies (Mueller and Pujol, 2001; Parrish and Van Arsdale, 2004; Csontos and Van Arsdale, 2008; Greenwood et al., 2016; Delano et al., 2018). The mean strike direction angle is 24 degrees smaller than the mean strike angle for the northern RF. This change in fault orientation is also observed in the prior studies. As is the case for the northern RF, zone 1 fault planes in Figure 10 suggest the presence of crosscutting faults. In this case, the faults are shallower than those that crosscut the northern RF and have a greater number of planes. Fault planes representing zones 1 and 2 (faults 23 and 24 in Table 1) are used in the final model.

4.2.1 Final Fault Model for the NMSZ

Faults with more than 200 modeled planes constitute the final fault model and are plotted in Figure 11. Figure 12 shows the fault model in different orientations. The fault parameters for the model are given in Table 1 and information for all modelled planes is presented in the Supporting Information (Table S3).

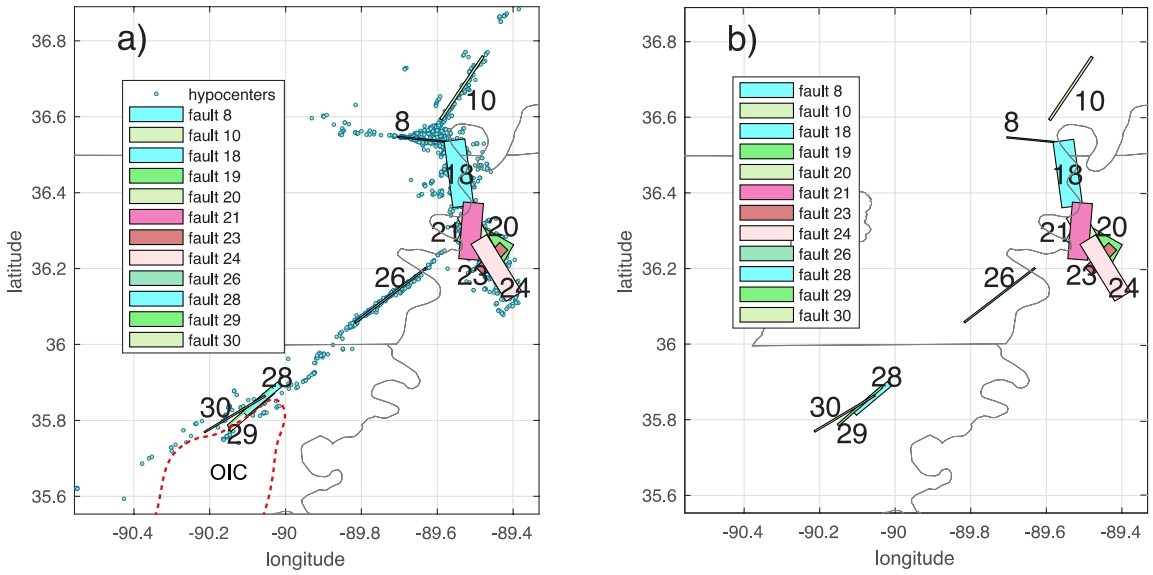

418

419 **Figure 11.** a) Final fault model for the NMSZ. Earthquakes are removed from the model in b).

420 Identified faults have more than 200 modeled planes. The fault numbers refer to the list in Table

421 S3 and in Table 1. Dashed contour is the outline of the Osceola intrusive complex (OIC) taken

422 from Hildenbrand et al. (2001).

423

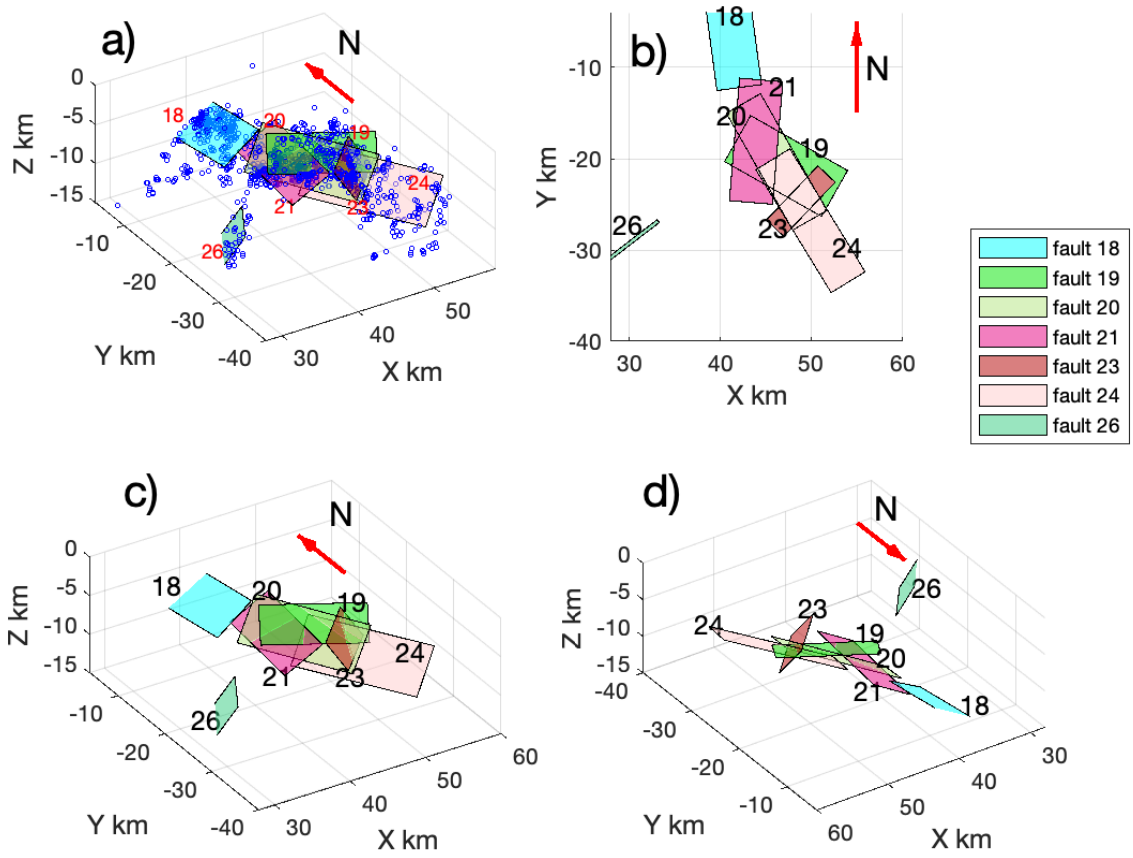

Figure 12. Blowup of the fault model for the RF. a) shows the distribution of hypocenters. b) is a map view. c) is a view looking toward the NE. Fault 26 is the AF. d) is a view toward SW.

Planes representing the strike-slip faults, WF, NF and AF, are clearly represented and are labeled 8, 10, and 26, respectively. Planes 18 and 24 represent the northern and southern RF thrust, respectively. The middle part of the RF has a complicated structure containing 4 planes labeled 19, 20, 21, and 23. Fault 21 connects with fault 18. These planes have strike angles that differ by about 13° but the same dip angles (Figure 12c). Plane 20 is the deepest fault in the central RF and is parallel to and overlaps plane 24 representing the southern RF. The strike and

dip angles of planes 20 and 24 differ by less than 2° and, from their orientation and dip angles, we suggest that they represent the main RF thrust surface (Figure 12 a, c, d). The continuity of faults 18, 21, 20 and 24 indicates a continuous thrust fault extending along the entire RF. However, fault 23 crosscuts central RF fault 20 and southern RF fault 24 (Figure 12d), implying that the RF is discontinuous. Fault plane 23 strikes N44°N and dips at an angle of 52°. This fault corresponds most closely to the Ridgley fault imaged in reflection profiles by Zoback (1979).

5 Discussion

The availability of a much larger dataset in our study resulted in a more precise image of the NMSZ fault structure than was possible in the hypoDD study by Dunn et al. (2010). Figure S11 provides a direct comparison between the hypoDD relocation results in Figure 3 and those determined by Dunn et al. (2010). Major improvements are better definition of the deeper structure on the RF and a very clear, vertical alignment of hypocenters along the northern segment of the AF. Additional earthquakes in our study closed the gap in seismicity near the intersection of the AF and the RF (Figure 3 cluster 6). Most of these earthquakes are aligned along the same trend as the well-defined portion of the AF but have shallower hypocenters, suggesting a change in fault structure near the intersection with the RF.

Modeled fault planes along the major strike-slip arms of the NMSZ (Figure 11) agree with previous published fault models. Our results confirm that these faults are near vertical and the fault strikes we determine lie within or just outside of the range of strikes found previously for these faults (Mueller & Pujol, 2001; Parrish and Van Arsdale, 2004; Csontos & Van Arsdale, 2008; Dunn et al., 2010; Pratt, 2012; Greenwood et al., 2016; Delano et al., 2018).

455 Our results for the southern part of the AF are intriguing. Seismicity in the southern part
456 of the AF is more diffuse than in the northern part but we have detected the presence of three
457 distinct faults (28, 29 and 30 in Figure 11). Two of these faults strike roughly parallel to the
458 northern part of the AF and one, fault 30, is oriented further east by about 10°. Two of the faults
459 have near-vertical dips and one (fault 28) has a shallower dip of 57°. According to Hildenbrand
460 et al. (2001), seismicity in the southern part of the AF is strongly affected by a major axial
461 intrusion called the Osceola intrusive complex (OIC in Figure 11); the presence of the OIC
462 produces scattered seismicity offset to the northwest from the trend of the northern AF and
463 clustering of earthquakes near the northern end of the intrusion. Our results indicate that
464 seismicity is less scattered than previously thought near the OIC and that distinct faults with
465 roughly the same orientation and dip as the northern part of the AF are present along the upper,
466 steeply-dipping northwest side of the intrusion. The intrusion may have followed preexisting
467 faults or, faults may have developed along the side of the intrusion in response to a concentration
468 of differential stress produced by the stronger, more rigid OIC. The latter explanation is favored
469 by Hildenbrand et al. (2001) and is compatible with other studies involving stress concentration
470 around large igneous intrusions (e.g., Ravat et al., 1987; Campbell, 1978).

471 The central portion of the RF has the most complicated fault structure, as has been noted
472 in previous studies (e.g., Muller and Pujol, 2001). Despite this complexity, there are SW dipping
473 planes that appear to connect with the planes depicting the northern and southern parts of the RF
474 (Figure 12, faults 18 and 24). The presence of the Ridgely fault (fault 23) breaks the continuity
475 of the RF. Segmentation of the RF implies that rupture may not continue unimpeded along its
476 entire length. Our results regarding the continuity of the RF differ from those of Greenwood et
477 al. (2016). These authors concluded that the RF was continuous across the Ridgely fault based on

similar amounts of displacement on stratigraphic markers on either side of the fault. A smaller amount of displacement was found south of the Ridgely fault and we suggest that the entire RF may rupture during large earthquakes such as the 1811-1812 sequence but the Ridgely fault may prevent rupture into the southern RF during smaller earthquakes.

Our final depiction of the NMSZ fault structure is an approximation, limited by our inability to model curved fault surfaces. This limitation did not affect our ability to model the straight, strike-slip segments of the NMSZ and our results add better defined fault dimensions for these segments. The RF is curved, as is obvious from Figure 3. Our plotted fault centers capture the curvature of the RF (Figure 7) but planes fit to the hypocenters produce the approximation indicated in Figure 11. Nonetheless, our model for the RF indicates continuity of the fault through the intersection with the AF and segmentation produced by the Ridgely fault. Our model can serve as a useful approximation of the RF in studies involving seismotectonics and rupture dynamics.

6 Conclusions

Relocation of 4568 earthquakes using HypoDD resulted in major improvement in the depiction of fault structure in the NMSZ. Three-dimensional structural variations along the Reelfoot fault are apparent. The northern portion of the Axial fault is very well defined; hypocenters do not exceed 10 km and become shallower near the intersection with the Reelfoot fault, indicating structural complexity.

OADC analysis of the relocated hypocenters produced a fault model consisting of 12, well resolved planes. The Reelfoot fault is continuous along strike from the northern end to the Ridgely fault. The Ridgely fault may serve as a barrier to rupture propagation along the entire

fault except for large earthquakes such as the 1811-1812 sequence. The southern end of the Reelfoot fault has a smaller strike angle and a greater dip than the northern portion of the fault, in agreement with prior studies. The strike-slip arms of the NMSZ are well resolved and correspond to near vertical planes. Three planes are resolved in the seismicity comprising the southern part of the Axial fault. These faults are located along the steeply dipping northwest side of the Osceola intrusive complex and may have formed in response to increased differential stress produced by the strong, rigid intrusion.

Data and Resources

All earthquake data are available at the U.S. Geological Survey Advanced National Seismic System (ANSS) Comprehensive Earthquake Catalog (ComCat) and the Center for Earthquake Research and Information (CERI) earthquake catalog. The HypoDD program and limiting parameters are decribed in Waldhauser (2001) HypoDD a program to compute double-difference hypocenter locations, USGS Open File Report 01-113. Reloacted hypocenters are available at http://dx.doi.org/10.17632/yjkykp3vms.1 (doi: 10.17632/yjkykp3vms.1).

Acknowledgments

This material is based upon work supported by the U.S. Geological Survey under Grant Number G19AP00052. The views and conclusions contained in this document are those of the authors and should not be interpreted as representing the opinions or policies of the U.S. Geological Survey. Mention of trade names or commercial products does not constitute their endorsement by the U.S. Geological Survey.

References

Boyd, O.S., Smalley, R., Jr., & Zeng, Y. (2015). Crustal deformation in the New Madrid seismic zone and the pore of postseismic stress. *Journal of Geophysical Research: Solid Earth*, *120*, doi:10.1002/2015HB012049.

Calais, E., & Stein, S. (2009). Time-variable deformation in the New Madrid seismic zone. *Science*, *323*(5920), 1442-1442.

Campbell, D. L. (1978). Investigation of the stress-concentration mechanism for intraplate earthquakes. *Geophysical Research Letters*, *5*(6), 477-479.

Cox, R. T., & Van Arsdale, R. B. (1997). Hotspot origin of the Mississippi embayment and its possible impact on contemporary seismicity. *Engineering Geology*, *46*(3-4), 201-216.

Cox, R. T., & Van Arsdale, R. B. (2002). The Mississippi Embayment, North America: a first order continental structure generated by the Cretaceous superplume mantle event. *Journal of Geodynamics*, *34*(2), 163-176.

Csontos, R., & Van Arsdale, R. (2008). New Madrid seismic zone fault geometry. *Geosphere*, *4*(5), 802-813.

Delano, J. E., Gold, R. D., Briggs, R. W., & Jibson, R. W. (2018). Coseismic sackungen in the New Madrid seismic zone, USA. *Geophysical Research Letters*, *45*(24), 13-258.

Dunn, M., DeShon, H. R., & Powell, C. A. (2013). Imaging the New Madrid Seismic Zone using double-difference tomography. *Journal of Geophysical Research: Solid Earth*, *118*(10), 5404-5416.

Dunn, M., Horton, S., DeShon, H., & Powell, C. (2010). High-resolution earthquake relocation in the New Madrid seismic zone. *Seismological Research Letters*, *81*(2), 406-413.

Fadugba, O. I. (2021). *Waveform and Geodynamic Modeling of Seismicity Associated with the Charlevoix Seismic Zone* (Doctoral dissertation, The University of Memphis).

Fadugba, O. I., Langston, C. A., & Powell, C. A. (2019). Better Constraining the Geometry of Faults in the Charlevoix Seismic Zone. *AGUFM, 2019*, S52C-08.

Frankel, A., Smalley, R., & Paul, J. (2012). Significant motions between GPS sites in the New Madrid region: Implications for seismic hazard. *Bulletin of the Seismological Society of America*, *102*(2), 479-489.

Greenwood, M. L., Woolery, E. W., Van Arsdale, R. B., Stephenson, W. J., & Patterson, G. L. (2016). Continuity of the Reelfoot Fault across the Cottonwood Grove and Ridgely Faults of the New Madrid Seismic Zone. *Bulletin of the Seismological Society of America*, *106*(6), 2674-2685.

Hao, Y., Magnani, M. B., McIntosh, K., Waldron, B., & Guo, L. (2013). Quaternary deformation along the Meeman-Shelby fault near Memphis, Tennessee, imaged by high-resolution marine and land seismic reflection profiles. *Tectonics*, *32*(3), 501-515.

Hardebeck, J. L. (2013). Geometry and earthquake potential of the Shoreline fault, central California. *Bulletin of the Seismological Society of America*, *103*(1), 447-462.

Hildenbrand, T. G., Stuart, W. D., & Talwani, P. (2001). Geologic structures related to New Madrid earthquakes near Memphis, Tennessee, based on gravity and magnetic interpretations. *Engineering Geology*, *62*(1-3), 105-121.

Hildenbrand, T.G., & Hendricks, J.D. (1995). Geophysical setting of the Reelfoot rift and relations between rift structures and the New Madrid seismic zone, *U.S. Geological Survey Professional Paper* 1538-E, 30 pp.

Horton, S. P., Kim, W. Y., & Withers, M. (2005). The 6 June 2003 Bardwell, Kentucky, earthquake sequence: Evidence for a locally perturbed stress field in the Mississippi embayment. *Bulletin of the Seismological Society of America*, *95*(2), 431-445.

568 Hough, S. E., Armbruster, J. G., Seeber, L., & Hough, J. F. (2000). On the modified Mercalli
569 intensities and magnitudes of the 1811–1812 New Madrid earthquakes. *Journal of*
570 *Geophysical Research: Solid Earth*, *105*(B10), 23839-23864.
571 Hough, S. E., Seeber, L., & Armbruster, J. G. (2003). Intraplate triggered earthquakes:
572 Observations and interpretation. *Bulletin of the Seismological Society of America*, *93*(5),
573 2212-2221.
574 Johnston, A. C. (1996). Seismic moment assessment of stable continental earthquakes, III: 1811–
575 1812 New Madrid, 1886 Charleston and 1755 Lisbon. *Geophys. J. Int*, *126*, 314-344.
576 Johnston, A. C., & Schweig, E. S. (1996). The enigma of the New Madrid earthquakes of 1811–
577 1812. *Annual Review of Earth and Planetary Sciences*, *24*(1), 339-384.
578 Kenner, S. J., & Segall, P. (2000). A mechanical model for intraplate earthquakes: Application to
579 the New Madrid seismic zone. *Science*, *289*(5488), 2329-2332.
580 Likas, A., Vlassis, N., & Verbeek, J. J. (2003). The global k-means clustering algorithm. *Pattern*
581 *recognition*, *36*(2), 451-461.
582 Mueller, K., & Pujol, J., (2001). Three-dimensional geometery of the Reelfoot blind thrust:
583 implications for moment release and earthquake magnitude in the New Madrid seismic zone.
584 *Bulletin of the Seismological Society of America*, *91*(6), 1563-1573.
585 Mueller, K., Champion, J., Guccione, M., & Kelson, K. (1999). Fault slip rates in the modern
586 New Madrid seismic zone. *Science*, *286*(5442), 1135-1138.
587 Ouillon, G., & Sornette, D. (2011). Segmentation of fault networks determined from spatial
588 clustering of earthquakes. *Journal of Geophysical Research: Solid Earth*, *116*(B2).

589 Ouillon, G., Ducorbier, C., & Sornette, D. (2008). Automatic reconstruction of fault networks
590 from seismicity catalogs: Three-dimensional optimal anisotropic dynamic clustering. *Journal*
591 *of Geophysical Research: Solid Earth*, *113*(B1).
592 Page, M. T., & Hough, S. E. (2014). The New Madrid seismic zone: Not dead
593 yet. *Science*, *343*(6172), 762-764.
594 Paige, C. C. (1982). LSQR: Sparse linear equations and least squares problems. *ACM Trans.*
595 *Math. Software*, *8*(1), 195-209.
596 Parrish, S., & Van Arsdale, R. (2004). Faulting along the southeastern margin of the Reelfoot
597 Rift in northwestern Tennessee revealed in deep seismic-reflection profiles. Seismological
598 Research Letters, 75(6), 784-793.
599 Pratt, T. L. (2012). Kinematics of the New Madrid seismic zone, central United States, based on
600 stepover models. *Geology*, *40*(4), 371-374.
601 Ravat, D. N., Braile, L. W., & Hinze, W. J. (1987). Earthquakes and plutons in the midcontinent-
602 Evidence from the Bloomfield pluton, New Madrid rift complex. *Seismological Research*
603 *Letters*, *58*(2), 41-52.
604 Thomas, W. A. (1991). The Appalachian-Ouachita rifted margin of southeastern North
605 America. *Geological Society of America Bulletin*, *103*(3), 415-431.
606 Thomas, W. A. (2006). Tectonic inheritance at a continental margin. *GSA today*, *16*(2), 4-11.
607 Tuttle, M. P., Schweig, E. S., Sims, J. D., Lafferty, R. H., Wolf, L. W., & Haynes, M. L. (2002).
608 The earthquake potential of the New Madrid seismic zone. *Bulletin of the Seismological*
609 *Society of America*, *92*(6), 2080-2089.

610 Tuttle, M. P., Wolf, L. W., Starr, M. E., Villamor, P., Lafferty III, R. H., Morrow, J. E., ... &
611 Haynes, M. L. (2019). Evidence for large New Madrid earthquakes about AD 0 and 1050
612 BC, central United States. *Seismological Research Letters, 90*(3), 1393-1406.
613 Van Arsdale, R. (2000). Displacement history and slip rate on the Reelfoot fault of the New
614 Madrid seismic zone. *Engineering Geology*, *55*(4), 219-226.
615 Waldhauser, F., & Ellsworth, W. L. (2000). A double-difference earthquake location algorithm:
616 Method and application to the northern Hayward fault, California. *Bulletin of the*
617 *Seismological Society of America*, *90*(6), 1353-1368.
618 Zhan, Y., Hou, G., Kusky, T., & Gregg, P. M. (2016). Stress development in heterogenetic
619 lithosphere: Insights into earthquake processes in the New Madrid Seismic
620 Zone. *Tectonophysics, 671*, 56-62.
621 Zoback, M.D. (1979). Recurrent faulting in the vicinity of Reelfoot Lake, northwestern
622 Tennessee. *Geological Society of America Bulletin,* 90,1019-1024.
623